

NUMERICAL ANALYSIS OF LASER SINTERING

ME5204 FINITE ELEMENT ANALYSIS (COURSE PROJECT)

J Jayagowtham
ME21B078

Said Anuj Jagannath
ME21B172

*Department of Mechanical Engineering,
Indian Institute of Technology Madras, Chennai - 600036, India.
me21b078@smail.iitm.ac.in, me21b172@smail.iitm.ac.in*

Abstract

The quasi stationary state solution of the two-dimensional Rosenthal equation for a moving gaussian heat source using finite element methods is studied in this project. The non linearity in the variation of thermal conductivity, density and specific heat with the temperature is accounted for using the Picard's iterative method. The weak form matrix computation is parallelized on account of their self sufficiency and independence. Adaptive mesh being finer near the Gaussian and coarser outside is used to effectively capture the temperature variations around the source .

Keywords: Rosenthal equation, Picard iterative method, Parallelization, Adaptive meshing

1 Introduction

Many manufacturing processes such as fusion welding, heat treatment, or forming by line heating involve the use of moving heat source. The earliest research on this problem is the modeling and analysis by Rosenthal. A finite element approach to the problem with fine meshing is often considered computationally expensive. The matrices involved are iteratively computed and assembled with complete independence, hence they can be parallelized. With adaptive meshing of fine mesh only around the source and relatively coarser mesh everywhere else, the computational time is significantly reduced.

In this study, the analysis of two-dimensional Rosenthal moving heat source using the Bubnov Galerkin finite element method for the setting described in [1] is carried out. Lagrange basis functions were the choice of weight functions in this study. An irregular mesh finer around the moving source and relatively coarser elsewhere was employed. In section 2, the problem is formulated with the necessary weak form equations. In section 3, the discretization approach is discussed in detail. In section 4, the code is validated with existing research papers and final results are presented. Section 5 concludes our work with remarks and observations. Section 6 is linked with the references for our work.

2 Governing equations and weak form

2.1 Strong Form of governing Heat Conduction Equation

The general form of the heat conduction equation is:

$$\rho c \frac{\partial T}{\partial t} = -\nabla \cdot \mathbf{q} + Q \quad (1)$$

According to Fourier's law, the heat flux is given by:

$$\mathbf{q} = -k \nabla T \quad (2)$$

From 1 and 2 we get:

$$\rho c \frac{\partial T}{\partial t} = \nabla \cdot (k \nabla T) + Q \quad (3)$$

For a heat source moving with velocity v along the x -axis, introduce a moving reference frame:

$$X = x + vt$$

From the equation 3 for heat conduction is expressed as:

$$\rho c \frac{\partial T}{\partial t} + v \rho c \frac{\partial T}{\partial x} - \nabla \cdot (k \nabla T) - Q = 0$$

For a quasi-stationary state, the time-dependent term $\frac{\partial T}{\partial t}$ vanishes, leading to the simplified **Rosenthal equation**:

$$v \rho c \frac{\partial T}{\partial x} - \nabla \cdot (k \nabla T) - Q = 0 \quad (4)$$

Where:

1. T : Temperature
2. ρ : Density of the material
3. c : Specific heat
4. v : Velocity of the moving heat source
5. k : Thermal conductivity
6. Q : Heat source term

2.2 Weak Form of governing Heat Conduction Equation

Expanding the the equation 4

$$v \rho c \frac{\partial T}{\partial x} - \frac{\partial}{\partial x} \left(k_x \frac{\partial T}{\partial x} \right) - \frac{\partial}{\partial y} \left(k_y \frac{\partial T}{\partial y} \right) - Q(x, y) = 0 \quad (5)$$

Using a test function $g(x, y)$, the weak form is obtained by multiplying the equation 5 by $g(x, y)$ and integrating over the domain Ω :

$$\int_{\Omega} g \left(v \rho c \frac{\partial T}{\partial x} \right) d\Omega - \int_{\Omega} g \frac{\partial}{\partial x} \left(k_x \frac{\partial T}{\partial x} \right) d\Omega - \int_{\Omega} g \frac{\partial}{\partial y} \left(k_y \frac{\partial T}{\partial y} \right) d\Omega - \int_{\Omega} g Q(x, y) d\Omega = 0$$

Applying Gauss divergence theorem to the second and third terms we get,

$$\begin{aligned}\int_{\Omega} g \frac{\partial}{\partial x} \left(k_x \frac{\partial T}{\partial x} \right) d\Omega &= \int_{\partial\Omega} g k_x \frac{\partial T}{\partial x} n_x dS - \int_{\Omega} \frac{\partial g}{\partial x} k_x \frac{\partial T}{\partial x} d\Omega \\ \int_{\Omega} g \frac{\partial}{\partial y} \left(k_y \frac{\partial T}{\partial y} \right) d\Omega &= \int_{\partial\Omega} g k_y \frac{\partial T}{\partial y} n_y dS - \int_{\Omega} \frac{\partial g}{\partial y} k_y \frac{\partial T}{\partial y} d\Omega\end{aligned}$$

On substituting, we get weak form for the corresponding differential equation 5 :

$$\underbrace{\int_{\Omega} g \left(v \rho c \frac{\partial T}{\partial x} \right) d\Omega}_{\text{Convection term}} + \underbrace{\int_{\Omega} \left(k_x \frac{\partial T}{\partial x} \frac{\partial g}{\partial x} + k_y \frac{\partial T}{\partial y} \frac{\partial g}{\partial y} \right) d\Omega}_{\text{Diffusion term}} - \underbrace{\int_{\Omega} g Q d\Omega}_{\text{Source term}} - \underbrace{\int_{\partial\Omega} g \left(k_x \frac{\partial T}{\partial x} n_x + k_y \frac{\partial T}{\partial y} n_y \right) dS}_{\text{Boundary term}} = 0 \quad (6)$$

2.3 Boundary Conditions

The boundary conditions are defined as follows:

1. **Prescribed temperature:**

$$T = T_D \quad \text{on } \Omega_D$$

2. **Heat flux:**

$$\mathbf{q} \cdot \mathbf{n} = q_N \quad \text{on } \Omega_N$$

Where:

1. T_h : Prescribed Temperature as 20°C (Equivalent to 293K)
2. \mathbf{n} : Surface normal vector
3. q_q : Heat flux given as 10^{-3} W/mm^3
4. Ω_D : Dirichlet boundary located at $x = 0 \text{ mm}$ on the rectangular slab, as shown in Figure 1.
5. Ω_N : Neumann boundary located at $x = 100 \text{ mm}$, $y = 0 \text{ mm}$, and $y = 100 \text{ mm}$ on the rectangular slab, as shown in Figure 1.

3 Discretization approach

To solve the heat conduction problem, the domain is irregularly discretized using triangular elements with an adaptive meshing strategy. The mesh is finer in the region surrounding the heat source and coarser elsewhere, as shown in figure 1:

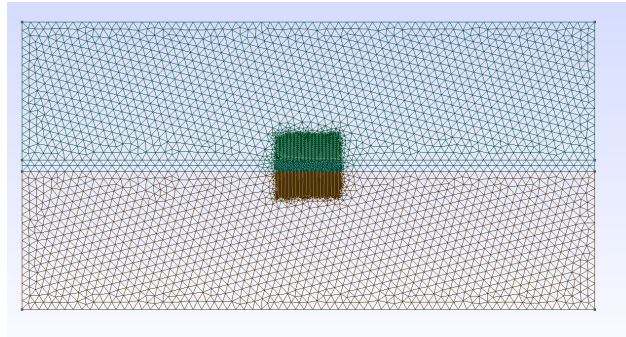


Figure 1: Mesh for source at $x = 50 \text{ mm}$ and $y = 25 \text{ mm}$

The triangular elements and associated shape functions are used to compute the system matrices.

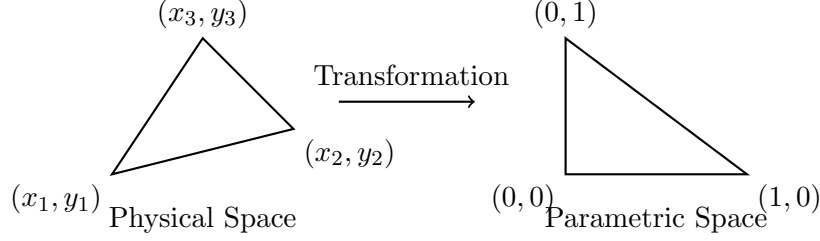
3.1 Element Type and Shape Functions

The small triangular elements have to be transferred to the parametric space in order to perform numerical integration over the domain using Gauss Quadrature.

$$\Phi_1 = 1 - \psi - \eta, \quad \Phi_2 = \psi, \quad \Phi_3 = \eta \quad (7)$$

where ψ and η are the transformed coordinates of a single triangular element inside of a unit cell.

The shape functions carry out following transformation,



From 7 it can be easily derived,

$$\begin{aligned} \frac{\partial \Phi_1}{\partial \psi} &= -1, & \frac{\partial \Phi_2}{\partial \psi} &= 1, & \frac{\partial \Phi_3}{\partial \psi} &= 0 \\ \frac{\partial \Phi_1}{\partial \eta} &= -1, & \frac{\partial \Phi_2}{\partial \eta} &= 0, & \frac{\partial \Phi_3}{\partial \eta} &= 1 \end{aligned}$$

Here, η and ϵ are the natural coordinates within the triangular element. The temperature $T(x, y)$ and test function $g(x, y)$ within an element are expressed as:

$$\begin{aligned} T(x, y) &= \phi_1 T_1 + \phi_2 T_2 + \phi_3 T_3 \\ g(x, y) &= \phi_1 g_1 + \phi_2 g_2 + \phi_3 g_3 \end{aligned} \quad (8)$$

3.2 Matrix Derivations for a Triangular Element

3.2.1 Diffusion Term:

Assuming isotropic material hence, we'll have $k_x = k_y = k$. The Diffusion term $\int_{\Omega} \left(k_x \frac{\partial T}{\partial x} \frac{\partial g}{\partial x} + k_y \frac{\partial T}{\partial y} \frac{\partial g}{\partial y} \right) d\Omega$ is expressed as:

$$\mathbf{K} = k \begin{bmatrix} \int_{\Omega} \left(\left(\frac{\partial \phi_1}{\partial x} \right)^2 + \left(\frac{\partial \phi_1}{\partial y} \right)^2 \right) d\Omega & \int_{\Omega} \left(\frac{\partial \phi_1}{\partial x} \frac{\partial \phi_2}{\partial x} + \frac{\partial \phi_1}{\partial y} \frac{\partial \phi_2}{\partial y} \right) d\Omega & \int_{\Omega} \left(\frac{\partial \phi_1}{\partial x} \frac{\partial \phi_3}{\partial x} + \frac{\partial \phi_1}{\partial y} \frac{\partial \phi_3}{\partial y} \right) d\Omega \\ \int_{\Omega} \left(\frac{\partial \phi_2}{\partial x} \frac{\partial \phi_1}{\partial x} + \frac{\partial \phi_2}{\partial y} \frac{\partial \phi_1}{\partial y} \right) d\Omega & \int_{\Omega} \left(\left(\frac{\partial \phi_2}{\partial x} \right)^2 + \left(\frac{\partial \phi_2}{\partial y} \right)^2 \right) d\Omega & \int_{\Omega} \left(\frac{\partial \phi_2}{\partial x} \frac{\partial \phi_3}{\partial x} + \frac{\partial \phi_2}{\partial y} \frac{\partial \phi_3}{\partial y} \right) d\Omega \\ \int_{\Omega} \left(\frac{\partial \phi_3}{\partial x} \frac{\partial \phi_1}{\partial x} + \frac{\partial \phi_3}{\partial y} \frac{\partial \phi_1}{\partial y} \right) d\Omega & \int_{\Omega} \left(\frac{\partial \phi_3}{\partial x} \frac{\partial \phi_2}{\partial x} + \frac{\partial \phi_3}{\partial y} \frac{\partial \phi_2}{\partial y} \right) d\Omega & \int_{\Omega} \left(\left(\frac{\partial \phi_3}{\partial x} \right)^2 + \left(\frac{\partial \phi_3}{\partial y} \right)^2 \right) d\Omega \end{bmatrix}$$

3.2.2 Convection Term:

This Convection term $\int_{\Omega} v \rho c \frac{\partial T}{\partial x} d\Omega$ is given by:

$$\mathbf{A} = v \rho c \begin{bmatrix} \int_{\Omega} \phi_1 \frac{\partial \phi_1}{\partial x} d\Omega & \int_{\Omega} \phi_1 \frac{\partial \phi_2}{\partial x} d\Omega & \int_{\Omega} \phi_1 \frac{\partial \phi_3}{\partial x} d\Omega \\ \int_{\Omega} \phi_2 \frac{\partial \phi_1}{\partial x} d\Omega & \int_{\Omega} \phi_2 \frac{\partial \phi_2}{\partial x} d\Omega & \int_{\Omega} \phi_2 \frac{\partial \phi_3}{\partial x} d\Omega \\ \int_{\Omega} \phi_3 \frac{\partial \phi_1}{\partial x} d\Omega & \int_{\Omega} \phi_3 \frac{\partial \phi_2}{\partial x} d\Omega & \int_{\Omega} \phi_3 \frac{\partial \phi_3}{\partial x} d\Omega \end{bmatrix}$$

3.2.3 Source term:

The source term $\int_{\Omega} gQ(x, y)d\Omega$ matrix is given by:

$$\mathbf{F} = \int_{\Omega} \begin{bmatrix} \phi_1 Q \\ \phi_2 Q \\ \phi_3 Q \end{bmatrix} d\Omega$$

3.2.4 Boundary Integral:

The boundary integral term becomes:

$$\mathbf{B} = \int_{\partial\Omega} \begin{bmatrix} \phi_1 \cdot (-q_o) \\ \phi_2 \cdot (-q_o) \\ \phi_3 \cdot (-q_o) \end{bmatrix} dS$$

Here, $\left(k_x \frac{\partial T}{\partial x} n_x + k_y \frac{\partial T}{\partial y} n_y\right)$ denotes the negative of the heat flux at the boundary.

Note : The gradients $\frac{\partial \phi_i}{\partial x}$ and $\frac{\partial \phi_i}{\partial y}$ are computed from the natural coordinates η, ϵ using the Jacobian transformation. The derivatives in physical coordinates $\frac{\partial \phi_i}{\partial x}$ and $\frac{\partial \phi_i}{\partial y}$ can be expressed using the Jacobian transformation as:

$$\begin{bmatrix} \frac{\partial \phi_i}{\partial x} \\ \frac{\partial \phi_i}{\partial y} \end{bmatrix} = \mathbf{J}^{-1} \begin{bmatrix} \frac{\partial \phi_i}{\partial \epsilon} \\ \frac{\partial \phi_i}{\partial \eta} \end{bmatrix}$$

where the Jacobian matrix \mathbf{J} and its inverse \mathbf{J}^{-1} are defined as:

$$\mathbf{J} = \begin{bmatrix} \frac{\partial x}{\partial \epsilon} & \frac{\partial y}{\partial \epsilon} \\ \frac{\partial x}{\partial \eta} & \frac{\partial y}{\partial \eta} \end{bmatrix}, \quad \mathbf{J}^{-1} = \frac{1}{\det(\mathbf{J})} \begin{bmatrix} \frac{\partial y}{\partial \eta} & -\frac{\partial x}{\partial \eta} \\ -\frac{\partial y}{\partial \epsilon} & \frac{\partial x}{\partial \epsilon} \end{bmatrix}$$

and the determinant of the Jacobian matrix is given by:

$$\det(\mathbf{J}) = \frac{\partial x}{\partial \epsilon} \frac{\partial y}{\partial \eta} - \frac{\partial x}{\partial \eta} \frac{\partial y}{\partial \epsilon}.$$

3.3 Meshing Procedure

An adaptive meshing strategy is used to capture the heat source region effectively. The mesh is finer in the region surrounding the heat source to resolve steep temperature gradients and coarser in regions away from the source for computational efficiency. The matrix computation was parallelized using **Multiprocessing.Pool** library from python making effective use of the multiple cores available in our systems alongside the independence of the iterations for the assembly.

4 Numerical Example

4.1 Problem Description

1. **Objective:** To compute the temperature distribution in the domain during laser sintering, accounting for the moving laser heat source, material properties, and boundary conditions.
2. **Domain:**

- (a) Size: A rectangular domain with dimensions:
- length** : 100 *mm*
 - breadth** : 50 *mm*
- (b) Properties: Titanium alloy Ti-6Al-4V, is assumed to have following properties:
- Thermal conductivity**:

$$k(T) = 3.276 \times 10^{-7}T + 0.0793 \text{ W/mm}\cdot\text{K}$$

- Specific heat** (assumed constant):

$$c_p(T) = 550 \text{ J/kg}\cdot\text{K}$$

- Density** (assumed constant):

$$\rho(T) = 2.116 \times 10^{-6} \text{ kg/mm}^3$$

3. Heat Source

- (a) **Model**: A Gaussian heat distribution simulates the laser's localized heating effect:

$$Q(x, y, t) = Q_{\max} \exp \left(-\frac{(x - x_s(t))^2 + (y - y_s(t))^2}{r^2} \right)$$

where:

- $Q_{\max} = 5 \text{ W/mm}^3$ is the maximum heat intensity.
 - $(x_s(t), y_s(t))$ represents the position of the moving laser at time t .
 - $r = 2 \text{ mm}$ is the radius of the laser beam.
- (b) **Velocity**: The laser moves at:

$$v = 2 \text{ mm/s}$$

along the $y = 25 \text{ mm}$ line.

Following figure 2 summaries the above described problem.

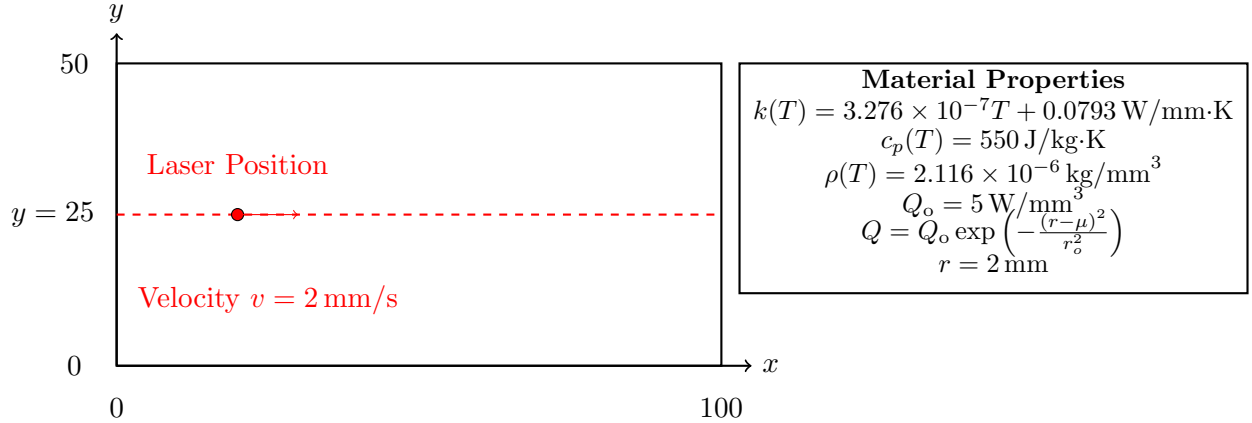


Figure 2: Schematic representation of the problem along with the given data.

As the thermal conductivity $k(T)$ depends on the temperature T , it is necessary to implement the **Picard iterative method** to handle the non-linearity. In order to validate the **matrices** computed, another research paper was referenced and the results matched.

4.2 Validation of codes

4.2.1 Validating Picard Iteration

To validate Picard we solved the following problem from the research paper [2].

1. **Problem Statement:** The problem involves transient nonlinear heat conduction in a square plate with the following specifications:

- (a) Size: A square domain with dimensions:

- i. **Length** : 100 *mm*
- ii. **Breadth** : 100 *mm*

- (b) Material Properties:

- i. **Density**, $\rho = 7000 \text{ kg/m}^3$.
- ii. **Specific heat**, $c_p = 465 \text{ J/(kg}\cdot\text{K)}$ (constant).
- iii. **Thermal conductivity**, $k(T) = 100 + (T - 50)^2 \cdot 0.004 \text{ W/m}\cdot\text{K}$.

- (c) Boundary Conditions:

- i. A constant temperature $T = 100^\circ\text{C}$ is applied on the bottom edge of the square plate.
- ii. The other edges are thermally insulated ($q = 0$).

- (d) Initial Condition:

$$T(x, y, t = 0) = 50^\circ\text{C}.$$

- (e) Heat Generation: The spatially varying heat generation rate is given by:

$$Q(x) = 15 \cdot \frac{x}{100} \left(1 - \frac{x}{100}\right) \cdot 10^6 \text{ W/m}^3.$$

- (f) Time Period: The simulation is conducted for $t = 10 \text{ s}$ with a time step $\Delta t = 0.1 \text{ s}$.

2. **Solution:** Following presents the approach used to solve the above given problem.

- (a) **Strong Form of the Governing Equation:** The governing equation for transient heat conduction with a nonlinear thermal conductivity is given as:

$$\rho c_p \frac{\partial T}{\partial t} - \nabla \cdot (k(T) \nabla T) = Q(x),$$

where:

- i. $T(x, y, t)$ is the temperature field.
- ii. ρ is the density of the material.
- iii. c_p is the specific heat capacity.
- iv. $k(T)$ is the temperature-dependent thermal conductivity.
- v. $Q(x)$ is the heat generation rate.

- (b) **Weak Form of the Governing Equation:** The governing heat conduction equation is given as:

$$\rho c_p \frac{\partial T}{\partial t} - \nabla \cdot (k(T) \nabla T) = Q.$$

To derive the weak form, we multiply the equation by the test function g and integrate over the domain Ω :

$$\int_{\Omega} \rho c_p \frac{\partial T}{\partial t} g d\Omega - \int_{\Omega} \nabla \cdot (k(T) \nabla T) g d\Omega = \int_{\Omega} Q g d\Omega.$$

Using the divergence theorem for the second term:

$$\int_{\Omega} \nabla \cdot (k(T) \nabla T) g d\Omega = \int_{\partial\Omega} k(T) (\nabla T \cdot \mathbf{n}) g d\Gamma - \int_{\Omega} k(T) \nabla T \cdot \nabla g d\Omega.$$

Applying boundary conditions ($\nabla T \cdot \mathbf{n} = 0$ on insulated edges), the weak form becomes:

$$\int_{\Omega} \rho c_p \frac{\partial T}{\partial t} g d\Omega + \int_{\Omega} k(T) \nabla T \cdot \nabla g d\Omega = \int_{\Omega} Q g d\Omega.$$

- (c) **Matrix Formulation:** Square domain was divided into triangular elements. For each element, following substitution was made $g = \sum_{i=1}^3 g_i \phi_i$ and $T = \sum_{i=1}^3 T_i \phi_i$. On substituting the weak form becomes,

$$\int_{\Omega} \rho c_p \frac{\partial T}{\partial t} g d\Omega + \int_{\Omega} k(T) \nabla T \cdot \nabla g d\Omega = \int_{\Omega} Q g d\Omega.$$

Substituting $g = \sum_{i=1}^3 g_i \phi_i$, where ϕ_i are the shape functions and g_i are the nodal values of g , the weak form is expressed as:

$$\sum_e \int_{\Omega_e} \rho c_p \frac{\partial T}{\partial t} \sum_{i=1}^3 g_i \phi_i d\Omega + \sum_e \int_{\Omega_e} k(T) \nabla T \cdot \nabla \sum_{i=1}^3 g_i \phi_i d\Omega = \sum_e \int_{\Omega_e} Q \sum_{i=1}^3 g_i \phi_i d\Omega.$$

Performing Time Discretization, Using an implicit backward Euler scheme for time discretization:

$$\frac{\partial T}{\partial t} \approx \frac{\mathbf{T}^{n+1} - \mathbf{T}^n}{\Delta t}.$$

Value of $\Delta t = 1 \text{ sec}$ was taken for above problem. The paper suggested 0.1 sec but we ran for both and got the same results. Then substituting $T = \sum_{i=1}^3 T_i \phi_i$ following is the matrix system obtained:

$$\left(\frac{\mathbf{M}}{\Delta t} + \mathbf{K}(\mathbf{T}^n) \right) \mathbf{T}^{n+1} = \mathbf{F} + \frac{\mathbf{M}}{\Delta t} \mathbf{T}^n. \quad (9)$$

where:

- i. **Mass Matrix (\mathbf{M}):**

$$\mathbf{M}_{ij} = \int_{\Omega} \rho c_p \phi_i \phi_j d\Omega,$$

which accounts for the transient term $\rho c_p \frac{\partial T}{\partial t}$.

- ii. **Stiffness Matrix ($\mathbf{K}(\mathbf{T})$):**

$$\mathbf{K}_{ij} = \int_{\Omega} k(T) \nabla \phi_i \cdot \nabla \phi_j d\Omega,$$

which incorporates the temperature-dependent thermal conductivity $\kappa(T)$.

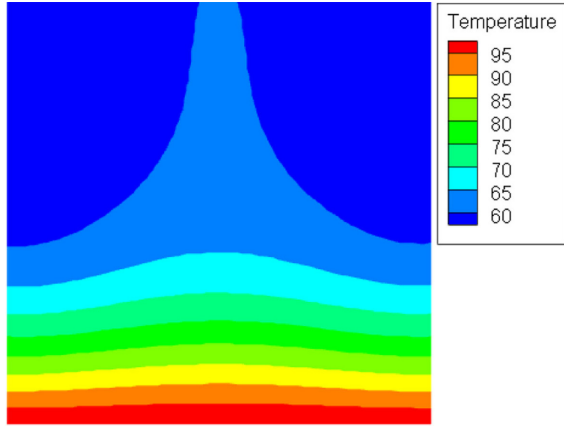
iii. **Load Vector (\mathbf{F}):**

$$\mathbf{F}_i = \int_{\Omega} Q \phi_i d\Omega,$$

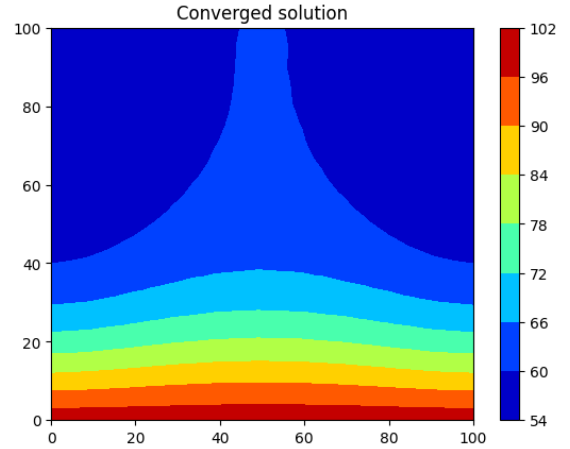
which represents the contribution of the heat source Q .

Solving equation 9, at $(n + 1)^{th}$ time-step needs to be done with the help of Picard iteration because of the dependence of thermal conductivity (k) with temperature. Once we get T^{n+1} for given T^n , we can solve Temperature till time $t = 10 \text{ sec}$, with the given Initial condition.

3. **Results:** Following is the comparison of solution obtained using Picard Iteration with the results obtained from paper [2].



(a) Solution from the reference paper.



(b) Solution obtained using Picard Iteration.

Figure 3: Comparison of the reference solution and the solution obtained using Picard Iteration.

Comparison of the Temperature values at two different nodes Node a (0,100) and Node b (100,100)

Table 1: Comparison of obtained and reference temperature values at nodes.

Node	Coordinates (mm)	Obtained Value (K)	Reference Value (K)	Difference (K)
a	(0, 100)	54.7433	54.746	0.0027
b	(100, 100)	54.7422	54.746	0.0038

4.2.2 Validating Matrices

For the problem discussed in section 6 consider following 2 cases with values of k , C_p and ρ ,

1. $\rho = 7.6\text{e-}6 \text{ kg/mm}^3$
2. $k = 0.025 \text{ W/mm.K}$
3. $C_p = 658 \text{ J/kg.K}$
4. $r_o = 2 \text{ mm}$
5. $v_o = 2 \text{ mm/s}$

6. $Q_o = 5 \text{ W/mm}^2$

1. **Case 1:** No source, Results in the following figure 6 are derived from the paper [1]

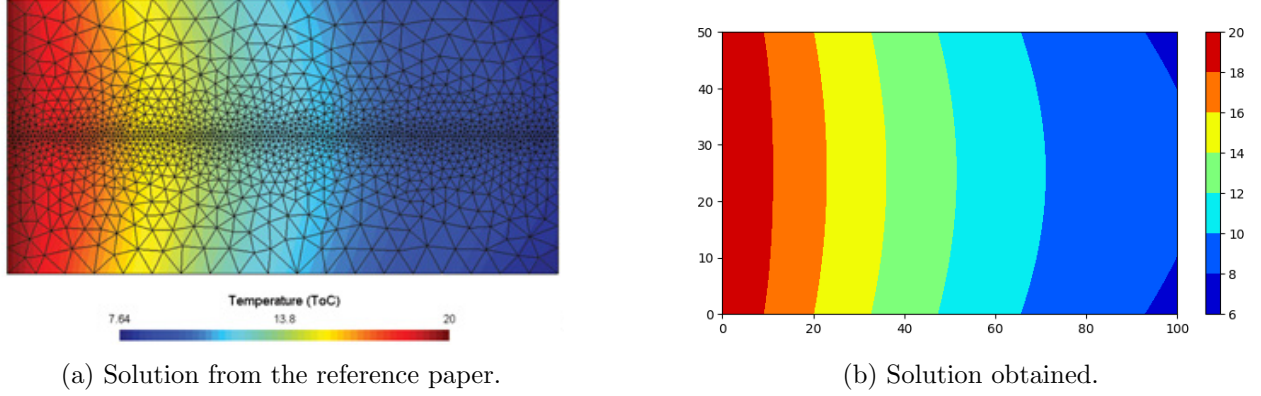


Figure 4: Comparison of the reference solution and the solution obtained.

It can be seen in the 4a, the minimum temperature is $T_{\min} = 7.64^\circ\text{C}$ while the maximum temperature is $T_{\max} = 20^\circ\text{C}$ (which is the boundary temperature as expected), and the obtained minimum temperature is $T_{\min} = 7.67^\circ\text{C}$ and maximum temperature is $T_{\max} = 20^\circ\text{C}$, which is quite near to the truth.

2. **Case 2:** Moving Source, Results in the following figure 5 are derived from the paper [3]

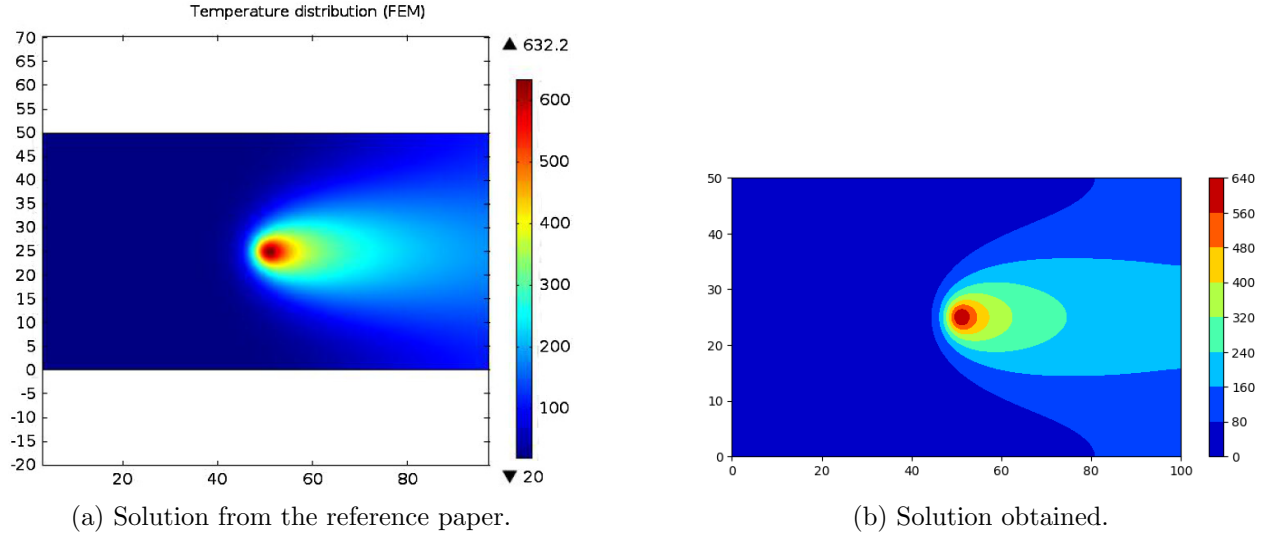


Figure 5: Comparison of the reference solution and the solution obtained.

It can be seen in the 5a, the minimum temperature is $T_{\min} = 20^\circ\text{C}$, while the maximum temperature is $T_{\max} = 632.2^\circ\text{C}$ and the obtained minimum temperature is $T_{\min} = 19.63^\circ\text{C}$ and maximum temperature is $T_{\max} = 630.49^\circ\text{C}$.

Thus, it is evident that the calculated matrices are correctly computed from solving and comparing the results with those obtained from two distinct problems, fool-proofing the code.

4.3 Mesh convergence

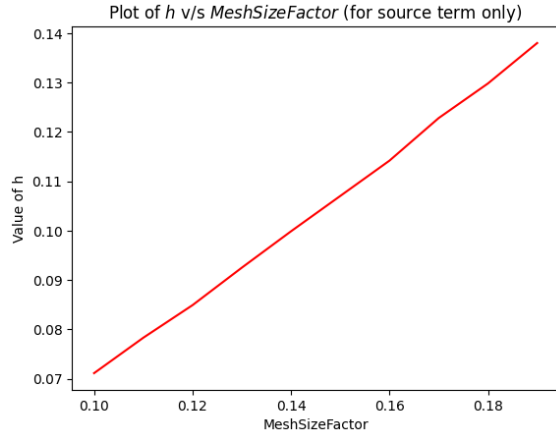
Mesh convergence was analyzed to ensure the solution's accuracy and computational efficiency:

1. **Image 6a:** Shows the variation of $h = \sqrt{\frac{A_{mean}^{ele}}{\text{Number of Elements}}}$ for the adaptive mesh's finer region, which captures the Gaussian heat source ($\sigma = 2$ mm). To resolve the source accurately, the mesh size h must satisfy $h \ll r_o$ (where $r_o = 2$ mm). An optimal mesh size factor of 0.15 was selected for the finer region, corresponding to $h \approx 1$ mm around 5% of 2 mm, ensuring sufficient resolution.
2. **Image 6b:** Illustrates the variation of temperature at a point near (50, 20) as a function of the mesh size factor for the coarser part of the domain, while keeping the finer region's mesh size factor fixed. The results show convergence of the temperature values as the mesh size factor approaches 1.0. Hence, choosing a mesh size factor of 1.0 for the coarser part is efficient and ensures accuracy.
3. **Image 6c:** Depicts the variation of temperature at the same point as a function of the total number of elements. The temperature stabilizes with increasing elements, confirming convergence and mesh independence. This further supports the choice of the mesh size factor.

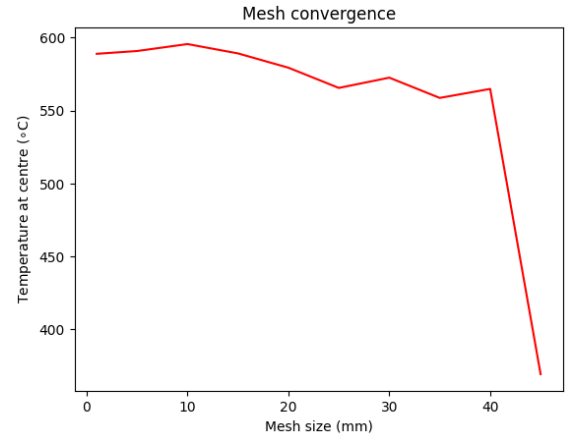
By selecting an adaptive mesh with a finer region mesh size factor of 0.15 and a coarser region mesh size factor of 1.0, the Gaussian heat source is accurately captured while maintaining computational efficiency. The results demonstrate that this configuration achieves a balance between precision and cost-effectiveness.

4.4 Solution

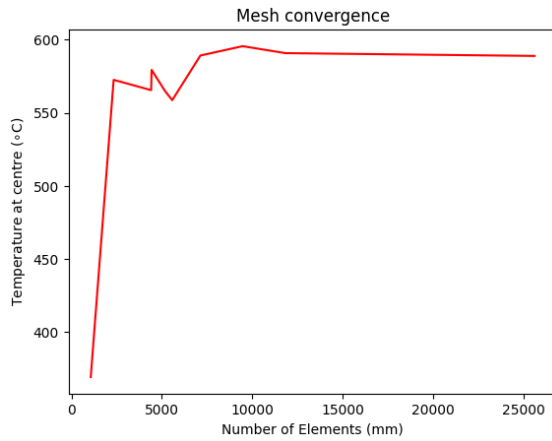
1. According to the Governing Equations in section 2 and Discretization Approach in section 3 following is the Temperature profile obtained for different source location as shown in Figure 7
2. **Inference:**
 - (a) **From Figure 7a:** The bright spot represents the heat source located at (75, 25), as indicated by the contour gradient. The boundary condition on the left edge is Dirichlet with $T = 20^\circ\text{C}$, resulting in uniform isotherms near this boundary. The other boundaries have Neumann boundary conditions ($q_o = 10^{-3} \text{ W/mm}^3$), leading to a vertical line in the contour near the boundary.
 - (b) **From Figure 7b and Figure 7c:** Both plots show the source location with similar temperature distributions. The Dirichlet boundary condition ($T = 20^\circ\text{C}$) at the left edge creates consistent isotherms near that boundary. The Neumann boundary conditions maintain a heat flux balance, producing a steady-state temperature distribution. Towards the left end the effect of the heat source is not felt, since it is Gaussian and dies away proportional to the square of the distance from the source.
 - (c) **Observation :** As the source moves towards the right end, the temperature surrounding the source increases when compared to the it being closer to the left boundary. Hence we can say that the Dirichlet condition has more impact in cooling the domain than the Neumann at the other 3 boundaries.



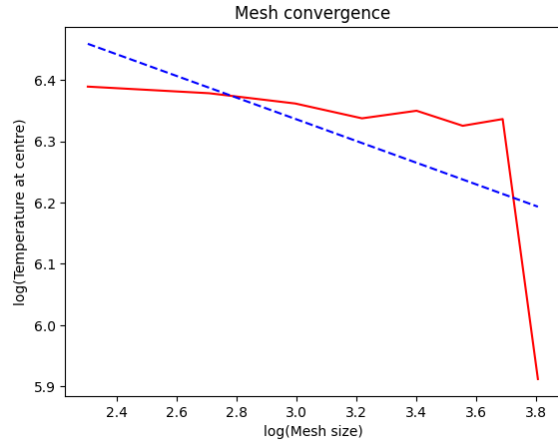
(a) h vs. mesh size factor for the finer region.



(b) Temperature vs. mesh size factor with source at (50, 20).



(c) Temperature vs. number of elements with source at (50, 20).



(d) Rate of convergence = 1.7 for the linear phase.

Figure 6: Mesh details plots.

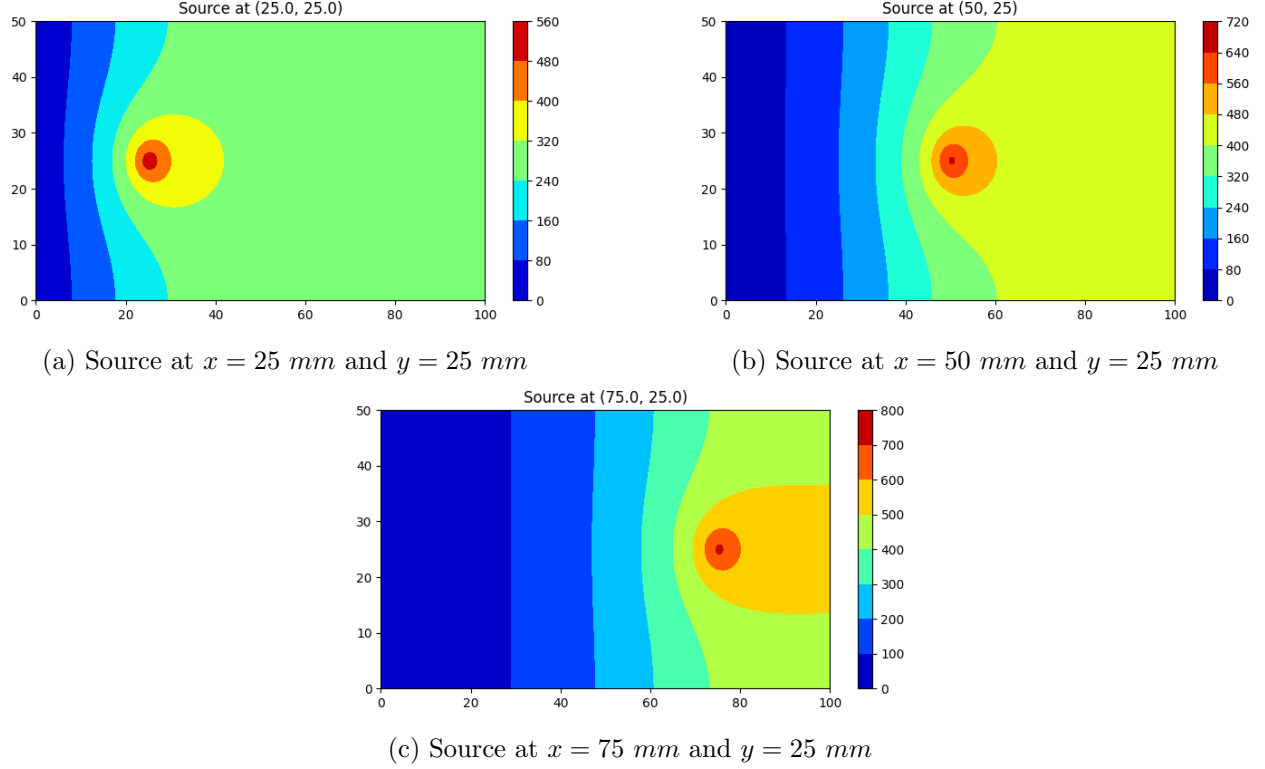


Figure 7: Comparison of the reference solution and the solution obtained.

4.5 Tackling Phase change problem (Additional):

1. **Differences observed in Phase change problem:** According the Governing Equations in section 2 and Discretization Approach in section 3, we considered the same problem with incorporation of phase change as discussed in the below mentioned paper [[4]]: From the paper , following is the deduced temperature data for phase changes 2

Table 2: Phase variation as a function of T

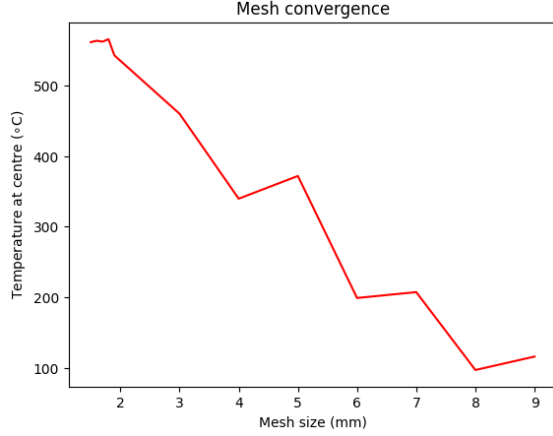
Temperature Description	Value (K)
T_β (β microstructure formation)	1268
T_l (Liquid formation)	1928
T_S (Solid formation)	1878
$T_{\alpha'S}$ (α microstructure from solidification)	1073
T_e (Evaporation, usually ignored)	3533

Variation of thermal properties as function of phase change and temperature as shown in 3

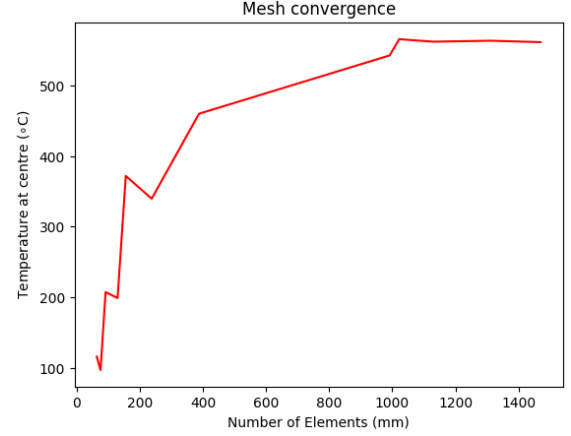
Table 3: Expressions for $\rho(T)$, $c_p(T)$, and $k(T)$ for different phases.

Phase	$\rho(T)$ (kg/m ³)	$c_p(T)$ (J/kg·K)	$k(T)$ (W/m·K)
α	$-5.13 \times 10^{-5}T^2 - 0.01935T + 4451$	$0.25T + 483$	$0.012T + 3.3$
β	$-2.762 \times 10^{-6}T^2 - 0.1663T + 4468$	$0.14T + 530$	$0.016T - 3$
Liquid	$-0.565T + 5093$	930	$0.0175T - 4.5$

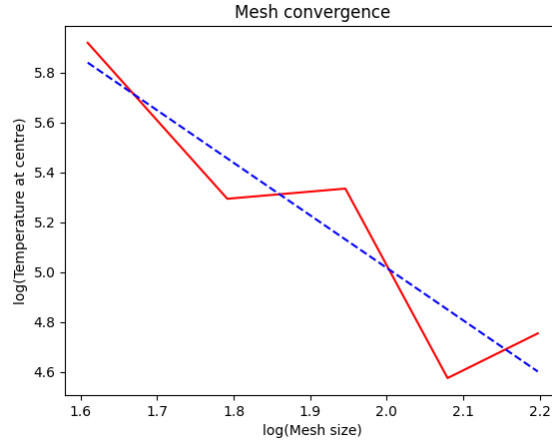
2. **Mesh Convergence:** With adaptive meshing, determining the phase of each element becomes challenging because the mesh changes between time steps and we need to interpolate to find the phase properties. To illustrate the method, a simple approach with a uniform mesh throughout the region is adopted mitigating the necessity of using an adaptive mesh but at the cost of lesser accuracy.



(a) Temperature vs. mesh size factor with source at (50, 25)



(b) Temperature vs. number of elements with source at (50, 25)



(c) Rate of convergence = 2.1

Figure 8: Normal Mesh details plots.

From the Figure 8,

- (a) **Image 8a:** Illustrates the variation of temperature at a point near (50, 20) as a function of the mesh size factor. The results show convergence of the temperature values as the mesh size factor approaches 1.0. Hence, choosing a mesh size factor of 1.0 for the coarser part is efficient and ensures accuracy.
- (b) **Image 8b:** Depicts the variation of temperature at the same point as a function of the total number of elements. The temperature stabilizes with increasing elements, confirming convergence and mesh independence. This further supports the choice of the mesh size factor.

3. **Results:** Following are the plots Figure 9 of source located at various locations in x for fixed $y = 25$ mm

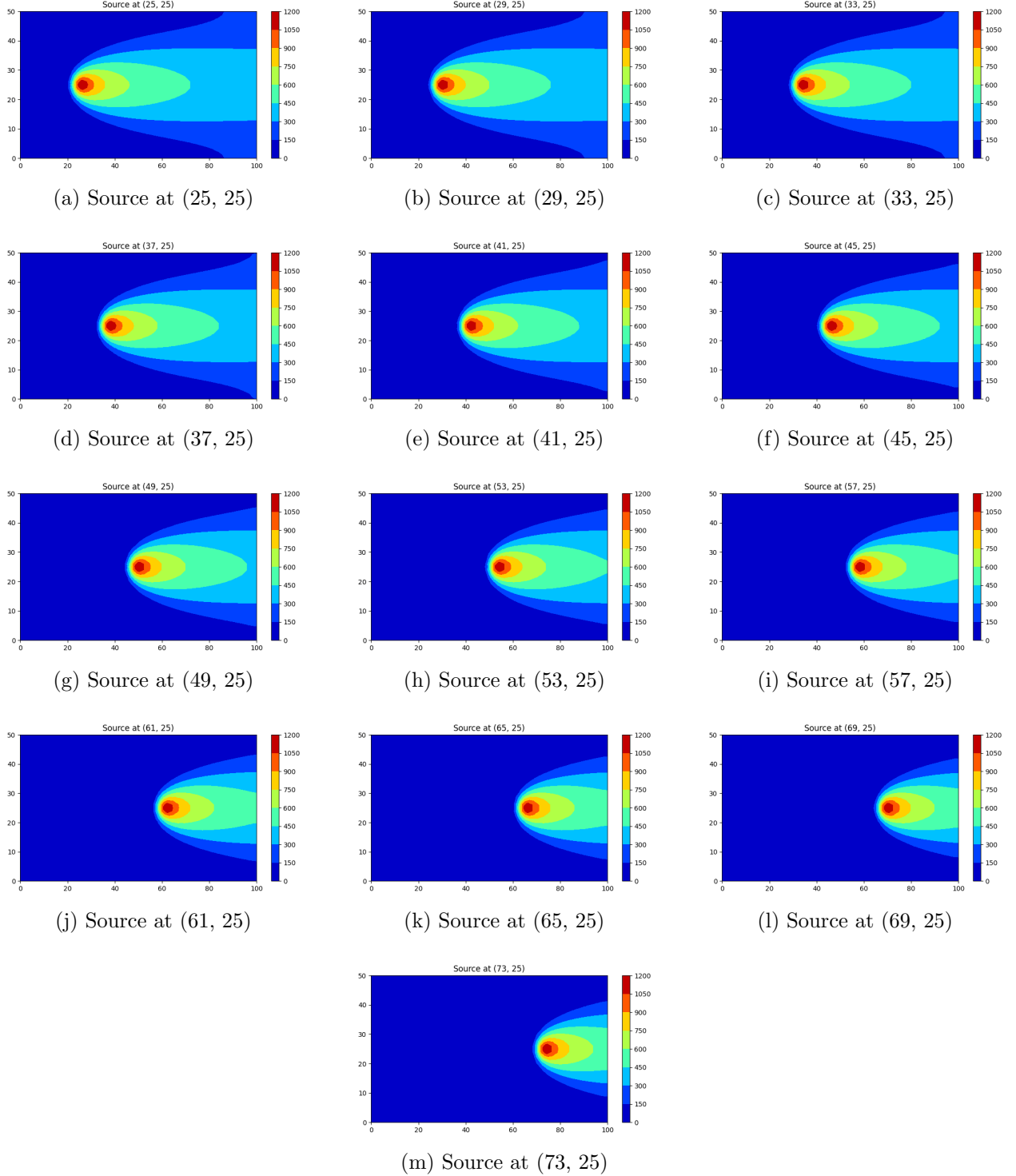


Figure 9: Contour plots of temperature distribution for varying source positions.

4. **Observations and Inferences:**

- (a) **Heat Distribution:** The temperature distribution follows a Gaussian profile centered at the moving source, with the highest temperature at the source's position.
- (b) **Thermal Diffusion:** Heat spreads predominantly in the direction of the source's movement, creating elongated, elliptical contours.
- (c) **Cooling Effect:** The thermal gradient behind the source reflects diffusion-dominated cooling as the source moves away.
- (d) **Practical Implications:** This system models dynamic heating scenarios, such as welding, laser-based heating, or moving heat sources in material processing applications.

5 Conclusions

We have successfully implemented the adaptive mesh based finite element solution for the Rosenthal equation. The parallelization boosted the speed of the iterations by 4 times. The adaptive meshing strategy reduced the number of elements further improving the computational speed. The consideration of micro structural phase change with normal meshing was done to show our method's robustness to any related modeling of a physical problem. For future work, the consideration of micro structural phase change for the titanium alloy can be incorporated. The only challenge here is that the old and new meshes are different and hence an optimal way to map the previous and current temperatures due to the moving source must be studied.

6 Individual contributions

Combined - Coding the matrix computations, validation of quasi-stationary solution, validation of Picard iteration, report writing

Jayagowtham - Parallelization of the matrices computation, Final code compilation

Said Anuj Jagannath - Automation of mesh generation, Adaptive mesh generation

7 References

- [1] Xuan-Tan Pham, *Two-Dimensional Rosenthal Moving Heat Source Analysis Using the Meshless Element Free Galerkin Method*, Numerical Heat Transfer, Part A: Applications, 63:11, 807-823, 2013. DOI: 10.1080/10407782.2013.757089,
- [2] L. Zhou, J. Lv, M. Cui, H. Peng, and X. Gao, *A polygonal element differential method for solving two-dimensional transient nonlinear heat conduction problems*, Eng. Anal. Bound. Elem., vol. 146, pp. 448–459, Jan. 2023. doi: 10.1016/j.enganabound.2022.10.017.
- [3] E. O. Reséndiz-Flores and F. R. Saucedo-Zendejo, *Two-dimensional numerical simulation of heat transfer with moving heat source in welding using the Finite Pointset Method*, Int. J. Heat Mass Transfer, vol. 90, pp. 239–245, 2015. doi: 10.1016/j.ijheatmasstransfer.2015.06.023.
- [4] K. Bartsch, D. Herzog, B. Bossen, and C. Emmelmann, *Material modeling of Ti-6Al-4V alloy processed by laser powder bed fusion for application in macro-scale process simulation*, Mater. Sci. Eng. A, vol. 814, Article 141237, Apr. 2021. doi: 10.1016/j.msea.2021.141237.